Mathematical Geosciences manuscript No.
(will be inserted by the editor)

Nonparametric estimation to reconstruct the deformation history of an active fold in the Caspian Basin

I.R. Sánchez-Borrego · J.I. Soto · M. Rueda · I. Santos Betancor

Received: date / Accepted: date

Abstract The complete shape of an active fold in the western margin of the South Caspian Basin has been established using a selected seismic section from a post-stacked seismic cube migrated in depth. The structure is an open anticline, which deforms a thick sequence (∼7 km) of Late Miocene to Pliocene sediments: the Productive Series (PS; 5.9 to ∼3.4-3.1 Ma). A major erosive unconformity separates the most recent sediments with onlap and draping geometries towards the anticline culmination.

Deformation is reconstructed using the complete fit of numerous seismic reflections by the nonparametric regression method. This has been implemented in the programming language R to estimate for example, the flanks dip, the folded areas of every deformed horizon, alike their length in both, the deformed and the pre-fold situation. It is inferred that this fold has a detachment surface located at 9.6 km depth.

The fold geometry resembles a detachment fold, although it is reconstructed a long-lived history of basinward tilting accompanying sedimentation and folding, which accelerated from 0.15°/Ma to 0.31°/Ma during deposition of the PS. Fold growth started at 3.5-3.4 Ma within the upper PS with a shortening rate of 0.2 mm/yr and coinciding with maximum sedimentation rates (3.24 mm/yr). Folding continued up-to-Present under lower sedimentation rates (av. 0.66 ±0.2 mm/yr) and a shortening rate that increased slightly from 0.17mm/yr

I. Sánchez-Borrego · M. Rueda
Departamento de Estadística e Investigación Operativa
Facultad de Ciencias, Campus de Fuentenueva, s/n, 18071 Granada, Spain.
Tel.: +34-958241000 ext. 20067
Fax: +34-958243267
E-mail: ismasb@ugr.es; mrueda@ugr.es

J.I. Soto · I. Santos Betancor
Departamento de Geodinámica and Instituto Andaluz de Ciencias de la Tierra (CSIC-Univ. Granada), Facultad de Ciencias, Campus de Fuentenueva, s/n, 18071 Granada, Spain.
E-mail: jsoto@ugr.es; idaira@ugr.es

at ∼3.1-to-1.6 Ma to 0.37-0.29 mm/yr during the last 1.6 Ma. The balance between sedimentation and shortening rates varies during folding, explaining the contrasting geometries observed in the growth sediments.

It is also inferred that volume was not conserved during deformation, possibly due to lateral flow of overpressured mud-rich sediments that inflated the fold core during shortening, similarly to the upwelling processes commonly described in salt-cored anticlines.

Keywords Detachment fold · shortening · nonparametric regression · local linear kernel regression · bandwidth.

1 Introduction

Nonparametric regression methods have been recently applied for estimating the regression function in a wide range of settings and areas of research. They are an attractive method, because of their flexibility and unlike their parametric counterparts, only weak assumptions over the regression function are made. Nonparametric regression methods do not need the regression model to be well-specified and a superior efficiency can be gained to the parametric ones, when the model is misspecified. As the regression model is typically unknown, the nonparametric smoother is likely to be a convenient choice for estimating the regression function.

There are several nonparametric regression methods available, such as kernel smoothing (Fan and Gijbels 1996; Ruppert and Wand 1994, among others), the penalized splines and semiparametric regression (Ruppert et al. 2003), wavelets (Antoniadis 1997; Percival and Walden 2000), among others. We use local polynomial regression as method of estimation, since it is well known for its good practical and theoretical properties (Fan 1992, 1993; Ruppert and Wand 1994) and can be easily adapted to the presence of discontinuities (Loader 1999; Sánchez-Borrego et al. 2006, among others).

The novelty of our analysis is that we apply these robust mathematical tools to characterize the geometry and to reconsturct the deformation history of a fold section. We use an anticline example from the SW Caspian Sea, using a 3D seismic dataset where the vertical scale is in depth. The selected section runs perpendicular to the fold axis and represents therefore a true fold profile (Ramsay and Huber 1987). To conduct any classification of the fold structure, to locate the position of the different fold elements, or to estimate the shortening and deformation histories, it is required a precise reconstruction of the folded surfaces (Fig. 1). In our case, we have conducted a detailed interpretation of the seismic image, exporting the position and depth of the different seismic horizons. We have used different statistical regression methods to fit the observations.

The studied fold resembles a detachment fold type, which is characterized by a competent folded sequence detached above a décollement surface or a weak layer (e.g., Chamberlin 1910; Dahlstrom 1990; Poblet and McClay 1996). The folding history is commonly reconstructed through the shortening

magnitude and different geometrical analyses can be done to estimate also the depth to the detachment surface (Fig. 1). In essence, shortening can be computed by two methods: (1) comparing the actual length of the folded surface with its original length in the undeformed situation, assuming that rock volume does not change during deformation (curvimetric shortening, S_C, e.g., Dahlstrom 1969); and (2) by the relationship between the area of structural relief of the deformed horizon and the horizon height above a reference surface (Epard and Groshong 1993). The latter shortening magnitude is commonly called as planimetric shortening (S_A, e.g., Gonzalez-Mieres and Suppe 2006). The different seismic horizons or reflections interpreted in the selected section have been fit by nonparametric methods and with these results we compute subsequently the S_C and S_A shortening values. We have also calculated how the shortening estimates, and consequently the folding history, are affected by the choice of the bandwidth parameter of the nonparametric regression smoother.

The main goal of our study is therefore to establish the best regression method for estimating the shortening magnitude in a fold example from the Caspian Sea depicted by seismic reflection profiling. We believe that this approach provides robust statistical tools to analyse easily other fold sections from any geological setting or scale.

2 Geological setting

The South Caspian Basin (SCB) is the southernmost basin of the Caspian Sea. It is located in South central Eurasia, within the offshore territories of Azerbaijan, Iran and Turkmenistan (Fig. 2). The SCB is a Tertiary intracontinental depression floored by a presumable Mesozoic oceanic crust, which is surrounded by numerous active fold-thrust belts, like the Caucasus, Talesh and the Kopeh Dagh (e.g., Neprochnov 1968; Berberian 1983; Mangino and Priestley 1998). The Caspian constitutes an important oil and gas productive region, representing around 3.4% and 1.8% of World production, respectively (Smith-Rouch 2006; EIA 2013).

The geodynamic evolution of the SCB is dominated by the Arabia-Eurasia collision that was initiated during the Late Mesozoic. The uplift of the Caucasus and the simultaneous N-directed thrusting of the northern Iran region are both responsible for the Pliocene-to-Present deformations that accompanied the rapid subsidence of the SCB (e.g., Nadirov et al. 1997; Allen et al. 2002; Brunet et al. 2003; Guest et al. 2007). Most of these deformations in the basin were accomplished by folding, which produced open anticlines. In the western margin of the SCB, anticline culminations vary progressively from NW-SE, in the onshore region, to NNW-SSE along the margin (e.g., Shikalibeily and Grigoriants 1980; Devlin et al. 1999). Folds show generally curved axial traces that may reflect strong variations along strike in the displacement and/or geometry of the associated, buried faults. Overpressured muds, which form diapiric structures with complex geometries, e.g., Christmas-tree mud diapirs,

intrude commonly these folds in the offshore regions (e.g., Fowler et al. 2000; Stewart and Davies 2006; Roberts et al. 2010).

The SCB is a super-deep basin containing around 20 km of sediments, deposited in a very rapidly subsiding basin from Jurassic to Present (e.g., Zonenshain and Le Pichon 1986; Nadirov et al. 1997). In the SCB it is particularly important the Maykop Formation because it constitutes the source rock for hydrocarbons. It was deposited during the Oligocene to Early Miocene (∼36 to 16 Ma) and consists of organic-rich shales (Hinds et al. 2004; Hudson et al. 2008). Basin subsidence, accompanied by rapid sedimentation, occurred since the Late Miocene promoting the accumulation of up to 10 km of Pliocene sediments, deposited in a lacustrine to deltaic environment (Jones and Simmons 1997; Inan et al. 1997; Abdullayev 2000; Morton et al. 2003; Hinds et al. 2004; Abreu and Nummedal 2007). These sediments constitute the so-called Productive Series (PS), which are formed by alterning sandstones and shales (5.9 to ∼3.4-3.1 Ma). The top of the PS is characterized by a regional erosional unconformity. Sediments deposited after the PS correspond to the Akchagyl (∼3.1-1.6 Ma), Apsheron (∼1.6-0.7 Ma) and Gelasian formations (<0.7 Ma) (e.g., van Baak et al. 2013; Forte et al. 2014). This latter group represents the terrigenous input provided to the basin by turbidity currents and slumps generated in a marginal shelf and are collectively grouped here as the post-PS series.

Rapid Miocene-to-Holocene burial contributed to the ideal scenario for the hydrocarbon production and preservation at great depocentres (e.g., Narimanov 1993). Discovered oil and gas deposits are generated in the Maykop Unit and are sited in the PS reservoirs, sealed by the intercalation of shale beds in the PS and by the post-PS group. The unconformity of the PS-top surface and fold culminations constitute also effective traps for hydrocarbons (e.g., Bagirov et al. 1997; Devlin et al. 1999). High sedimentation rates resulted in excessive fluid pressure within the undercompacted mud-rich Maykop sediments triggering mud diapirism (e.g., Buryakovsky et al. 1995; Yusifov and Rabinowitz 2004).

3 Fold section dataset

This contribution is based on the study of a 3D seismic block combined with the geophysical information obtained from two exploratory wells. REPSOL Exploración S.A. has provided the complete dataset for this study. The seismic cube is located in the western margin of the SCB, South of the Kura River mouth, in offshore Azerbaijan with water depths between 30 and 150 m (Fig. 2).

We have studied an anticline structure cored by mud, through the seismic interpretation of a post-stacked seismic cube migrated in depth. The grid covers approximately 653 km^2 and extends to 9 km depth. 3D seismic interpretation has been conducted with the KingdomSuite software and has been

correlated with the logging and chrono-stratigraphic information provided by the nearby wells.

From the resultant 3D interpretation, we have selected a representative seismic section, which runs perpendicular to the fold axis. This section trends SW-NE, has a vertical scale in depth (Fig. 3) and corresponds therefore to a true fold profile (Ramsay and Huber 1987).

Interpretation has been carried through picking several seismic reflections with contrasting amplitudes and seismic characteristics. We have identified two major sedimentary sequences, PS and post-PS, separated by a marked and regional, erosive unconformity (PS-t in Fig. 3). The bottom of the PS sequences has been placed tentatively according to well information and following a seismic package with high amplitudes (PS-b in Fig. 3). Within the PS sequences, we have distinguished ten seismic reflections, named as H1 to H10. Within the post-PS package, the internal structure of the Akchagyl (top of the unit Ak1) and Apsheron (top Ap1) units has been also characterized through two additional continuous reflections, which are labelled as Ak2 and Ap2.

The overall seismic horizons shown in Figure 3 have been fitted in 3D with the seismic interpretation software. This vertical slice of the resulting grids has been exported individually as x (longitude)-y (latitude)-z (depth) data. These distributions have been fitted with different functions, particularly with the nonparametric estimation method, looking for the best method to reconstruct the complete shape of the folded horizons.

4 The nonparametric estimation method

Let (x_i, Z_i) be a set of observations from the tridimensional variable $(\text{longitude}, \text{latitude}, Z)$, being Z the depth and X the horizontal distance computed from the latitude and longitude coordinates. If observations satisfy the regression model

$$Z_i = m(x_i) + \varepsilon_i, \qquad i = 1, \ldots, n, \tag{1}$$

where $m(\cdot)$ is the unknown regression function defined within the interval $[0, 1]$, and the errors ε_i are independent and identically distributed with mean of zero and constant variance σ^2. We assume that the $(p+1)$-th derivative of m at point x exists. The unknown regression function is then locally approximated by a polynomial of order p. In a neighbourhood of x, we use a Taylor expansion of m at point x and fit locally the resulting polynomial by solving a weighted least squares regression problem.

The solution to the above-mentioned problem is given by $\widehat{\beta} = (X^t W X)^{-1} X^t W z$, where $X = [1 \quad (x_i - x)]_{i=1}^n$ is the design matrix, $z = [Z_i]_{i=1}^n$ and $W = diag\{K_h(x_i - x)\}$, where h is the bandwidth parameter controlling the size of the local neighborhood and $K_h(\cdot) = K(\cdot/h)/h$ with K a kernel function, usually a symmetric probability density function with bounded support. Finally the regression function is estimated by

$$\widehat{m}_h(x) = e_1^t \left(X^t W X + diag\{\delta/n^2\} \right)^{-1} X^t W z, \tag{2}$$

with $e_1^t = (1, 0)$ and for small appropriate $\delta > 0$. This adjustment was also used in Breidt and Opsomer (2000) in the survey context and previously in Fan (1993).

The role of the bandwidth parameter is critical to the performance of the nonparametric regression estimator. One of the most popular methods for selecting the bandwidth parameter h is by minimizing the cross-validation score defined by

$$CV(h) = n^{-1} \sum_{j=1}^{n} (Z_j - \widehat{m}_{h,-j}(x_j))^2,$$

where $\widehat{m}_{h,-j}(x_j)$ is the estimator $\widehat{m}_h(x_j)$ where the observation (x_j, Z_j) is left-out.

In principle, estimator (2) can be undefined. If there are few observations in the support of the kernel at some x, then the matrix $X^t W X$ will be singular. This is not a problem in practice, because it can be avoided by selecting a bandwidth that is sufficiently large to make $X^t W X$ invertible at all locations.

This method of estimation works under the assumption that regression functions are smooth. This assumption results in smooth estimations of the regression functions, but these tend to show considerable bias if any discontinuities are present.

Sánchez-Borrego et al. (2006) proposed a local linear kernel estimator in the general infinite population context taking into account jump points. Following the assumption of finite population, it is proposed an adapted kernel smoother for estimating the underlying discontinuous regression function of the SCB depth data.

This method is the result of combining a modified projected observations procedure, first introduced by Wu and Chu (1993), together with the local linear kernel smoother. The method of estimation consists of two steps: we first estimate the jump points, and secondly, the regression function is estimated using these estimated jump points.

If the regression function m is continuous everywhere but in a finite known number of jump points q, we write these points as t_k $(k = 1, \ldots, q)$.

The method of projected observations reuses the available data in order to add new observations to the jump points, contributing to improve the estimation of the regression function in these regions. To estimate the jump points we consider the following estimator:

$$\widehat{m}_h(x) = \frac{\sum_{\{i:x_i \in [-1,2]\}} K_h(x - x_i)\{s_{n,2} - (x - x_i)s_{n,1}\} Z_i^P}{\sum_{\{i:x_i \in [-1,2]\}} s_{n,2}s_{n,0} - (s_{n,1})^2 + \delta/n^2}, \qquad (3)$$

where K is a kernel function, $s_{n,j} = \sum_{\{i:x_i \in [-1,2]\}} K_h(x - x_i)(x - x_i)^j$ and x_i is the pseudo-point. This is constructed from the original design point with the locations of the projected observations at the first projection interval

$$x_i = (-1)x_{1-i} \qquad i = 2 - n, 2 - n + 1, \ldots, 0.$$

and

$$x_i = 2 - x_{2n-i+1} \qquad i = n+1, n+2, \ldots, 2n-1,$$

are the pseudo-points in the second projection region. The corresponding projected observation Z_i^P is given by

$$Z_i^P = \begin{cases} Z_{2-i} + 2\widehat{m}_{gL}(0)(x_i) & i = 2-n, 2-n+1, \ldots, 0, \\ Z_i & i = 1, 2, \ldots, n, \\ Z_{2n-i} + 2\widehat{m}_{gR}(1)(x_i - 1) & i = n+1, n+2, \ldots, 2n-1, \end{cases}$$

where $\widehat{m}_{gL}$ and $\widehat{m}_{gR}$ are two kernel Priestley and Chao (1972) smoothers which involve different kernel functions, L and R, given by $L(x) = (-6 - 12x)$ and $R(x) = (-1)L(-x)$, and a pilot bandwidth, $g = 1.572h$
We consider the difference function, $D(\cdot) = \widehat{m}_1(\cdot) - \widehat{m}_2(\cdot)$, where $\widehat{m}_1(\cdot)$ and $\widehat{m}_2(\cdot)$ are estimators like (3) with the same bandwidth but different kernel functions, K_1 and K_2. The common bandwidth is selected by the usual cross-validation procedure.

Finally the jump points are estimated by

$$\widehat{t}_k = \max_{x \in A_k} |D(x)| \qquad k = 1, \ldots, q,$$

where A_k is given by

$$A_k = [h, 1-h] - \bigcup_{j=1}^{k-1} [\widehat{t}_j - \delta, \widehat{t}_j + \delta] \qquad k = 1, \ldots, q,$$

δ being a constant close to zero, and h the bandwidth selected by cross-validation.

To estimate the discontinuous regression function we consider a modification of the projected observations mentioned above. We consider that $\widehat{t}_{k-1} \leq \widehat{t}_k$, for $k = 1, \ldots, q+1$, defining $t_0 = 0$ and $t_{q+1} = 1$. The projected observations are given by

$$\begin{aligned} Z_i^{pk} &= Z_{2-i} + 2\widehat{m}_{gL}(x)(x_i - \widehat{t}_k) \qquad i = 2-n, 2-n+1, \ldots, 0 \\ Z_i^{pk} &= Z_{2n-i} + 2\widehat{m}_{gR}(x)(x_i - \widehat{t}_{k-1}) \qquad i = n+1, n+2, \ldots, 2n-1, \end{aligned} \tag{4}$$

and $Z_i^{pk} = Z_i$ for $i = 1, \ldots, n$. The pseudo-points, the pilot bandwidth g and the kernel functions $\widehat{m}_{gR}$ and $\widehat{m}_{gL}$ follow the previous mentioned considerations. Finally, for each $k = 1, \ldots, q+1$ and $x \in [\widehat{t}_{k-1}, \widehat{t}_k]$, we estimate the regression function by using

$$\widehat{m}_h(x) = \sum_{k=1}^{q+1} \sum_{\{i: X_i \in [2\widehat{t}_{k-1} - \widehat{t}_k, 2\widehat{t}_k - \widehat{t}_{k-1}]\}} \frac{K_h(x - x_i)\{s_{n,2} - (x - x_i)s_{n,1}\}Z_i^{pk}}{s_{n,2}s_{n,0} - (s_{n,1})^2},$$

where Z_i^{pk} are the projected data obtained from the original observations Z_i at the design points $x_i \in [\widehat{t}_{k-1}, \widehat{t}_k]$. The $s_{n,j}$ are given by:

$$s_{n,j} = \sum_{\{i:x_i \in [2\widehat{t}_{k-1} - \widehat{t}_k, 2\widehat{t}_k - \widehat{t}_{k-1}]\}} K_h(x - x_i)(x - x_i)^j.$$

4.1 Error estimation

We have considered two main methods of estimation: the nonparametric local polynomial regression and the classical parametric regression. We use $\widehat{m}_{\mathrm{np}}$ and $\widehat{m}_{\mathrm{par}}$ to denote the nonparametric and the parametric estimators, respectively.

The comparison between these methods will be made in terms of the gain in efficiency through the R_1, and R_2 percentages, which are given by

$$R_1(\widehat{m}_{\mathrm{np}}) = \left(\frac{\sqrt{\frac{1}{n}\sum_{i=1}^{n} \left(Z_i - \widehat{m}_{\mathrm{par}}(x_i)\right)^2}}{\sqrt{\frac{1}{n}\sum_{i=1}^{n} \left(Z_i - \widehat{m}_{\mathrm{np}}(x_i)\right)^2}} - 1 \right) \times 100, \tag{5}$$

and

$$R_2(\widehat{m}_{\mathrm{np}}) = \left(\frac{E_2(\widehat{m}_{\mathrm{par}})}{E_2(\widehat{m}_{\mathrm{np}})} - 1 \right) \times 100. \tag{6}$$

In where $E_2(\widehat{m}_{\mathrm{np}})$ and $E_2(\widehat{m}_{\mathrm{par}})$ are the length of the estimated folded surface,

$$E_2(\widehat{m}_{\mathrm{np}}) = \sum_{i=1}^{n-1} \left| \Delta_{1i} + \Delta_{2i} \right|, \tag{7}$$

with Δ_{1i} and Δ_{2i} given by

$$\Delta_{1i} = \sqrt{(x_{i+1} - x_i)^2 + (\widehat{m}_{\mathrm{np}}(x_{i+1}) - \widehat{m}_{\mathrm{np}}(x_i))^2}, \tag{8}$$

and

$$\Delta_{2i} = \sqrt{(x_{i+1} - x_i)^2 + (Z_{i+1} - Z_i)^2}. \tag{9}$$

5 Fold elements

Using the smoothed distribution obtained with the nonparametric regression method, the geometry of the folded surfaces has been characterized through the following parameters. They are shown schematically in Figure 4 and their abbreviations and significance are detailed in 1.

For every surface, we estimate the position and magnitude of the maximum and minima of the distribution. They correspond to the fold crest domain in the anticline and the trough domain in the nearby synclines, respectively. Between them, it has been estimated subsequently the position of the inflection points, which coincide with the regions with a change in the concavity of the fold flank. Around these inflection points, we have calculated the best linear

fit of the distribution and its angle to the horizontal that is considered a good estimate of the attitude of the fold flank (β_i).

For any reconstruction of the folding history, it is crucial to reconstruct accurately the position of the regional surface (e.g., Fig. 1); i.e., the line in two-dimensions that constitutes the lower boundary of the fold or the depth of the lower detachment surface, H_{det}. The position of this line will condition the shortening magnitude (S_C and S_A) (e.g., Mitra 2002; Wiltschko and Groshong 2012). After exploring different fits to this surface or line in the fold section, we have found that the best parametric method to estimate the regional is the linear regression connecting the two extreme domains of the fold (Fig. 4). For every folded surface, we have established this line, measuring its length (L_f), dip (α_{ref}), and registering the coefficient of determination of the linear regression (r^2). The folded areas above and below this regional have been also measured, alike the total length of the folded surface (L_i) (e.g., Figs. 4, 6).

Following Dahlstrom (1969), the curvimetric shortening (S_C) associated to the fold is given by:

$$S_C = L_i - L_f. \tag{10}$$

Additionally, the other magnitude to estimate shortening is given by the planimetric shortening (S_A), by:

$$S_A = \frac{\sum A_i}{H_i}, \tag{11}$$

where H_i is the relative elevation of the folded horizon above a reference surface, and $\sum A_i$ is obtained by subtracting the areas beneath the regional (A_1 and A_3 in Fig. 4) to the total area above it (Mitra and Namson 1989; Epard and Groshong 1993; Mitra 2003; Gonzalez-Mieres and Suppe 2006). We have used the bottom of the Productive Series (PS-b) as the reference surface for measuring relative elevations (Figs. 3 and 5). Our analysis follows the method developed by Gonzalez-Mieres and Suppe (2011) to reconstruct the growth history of a fold and is summarized graphically in Figure 1. For the growth section, the equation (11) is modified to the following expression:

$$S_A = \left(\frac{dA}{dH}\right)_{growth} + H_{det}\frac{dS}{dH}. \tag{12}$$

In this case the height should be measured with respect to the detachment surface (H_{det}) and the dS/dH corresponds to the ratio between the shortening rate (dS/dt) to the sedimentation rate (dH/dt) (Gonzalez-Mieres and Suppe 2011). In these ratios, dS is computed using the S_A estimated through the area-to-depth relationship (Fig. 1).

The overall calculations conducted for this study have been carried out with the R software. Nowadays, there are some available methods in R for estimating the continuous regression function. We have written our own code in R for estimating the discontinuous regression function. Thus, the nonparametric estimation and the overall calculations conducted for this fold dataset can be routinely computed using this implemented tool. Programming details are available upon request from the authors.

6 Results

The complete shape of the studied fold from the South Caspian Basin (SCB) shown in Figure 3 has been estimated using nonparametric regression, and the different geological magnitudes computed with our software are listed in Table 2.

Within the studied seismic cube in the western margin of the SCB (Fig. 2), we have selected this fold profile because it shows a complete and continuous section of the fold structure, and it lacks of any significant fault and of any of the abundant mud diapirs occurring in the area. The fold geometry is also a good representation of the complete structure and corresponds to a box-like anticline, with a broad anticline crest that narrows downwards, within the Productive Series (Fig. 3). In the same direction, the interlimb angle diminishes and the fold becomes more pointed.

The overall geometry of the fold describes, in principle, two major sequences with contrasting differences. The complete section formed by the Productive Series (PS), from the PS-bottom to PS-top reflections, seems to maintain the stratigraphic thickness from one flank to the other. The most recent sequences, bounded by the PS-top and the seafloor, in the other hand, thin significantly towards the anticline crest. According to these general observations, they could mark the pre- and syn-growth epoch of folding, respectively. Hereafter, our description of the results looks for a better reconstruction of the folding history and a precise estimate of the shortening magnitude.

The description of our results is divided in two sections. Firstly, we summarize our approach to a better reconstruction by nonparametric estimation of the fold, and secondly, our results regarding the folding magnitudes and deformation history.

6.1 Fold reconstruction by nonparametric regression

We have considered three different approaches to estimate the depth data of the anticlines: the piecewise local linear kernel smoother (Fan and Gijbels 1996; Ruppert and Wand 1994, among others), the adapted to discontinuities local linear kernel smoother (Sánchez-Borrego et al. 2006) and the classical parametric regression estimator. We consider the best parametric function in terms of the coefficient of determination value, making sure that relevant coefficients involved in the model are significantly non-zero.

The adapted to discontinuities kernel smoother is considered when jump points are detected. To detect them we have used the method of Bowman et al. (2006), that is implemented with the package sm in the R software.

Once the discontinuities are detected, the jump points and the discontinuous regression function are estimated using Sánchez-Borrego et al. (2006) method.

Graph on the right hand side of Fig. 5 shows the PS-bottom estimated surface and two jump points detected by the above-mentioned method. The

detected jump points are estimated and the discontinuous regression function is estimated by the adapted to discontinuities kernel smoother, which makes use of the estimated jumps.

The choice of the bandwidth is a critical issue when smoothing techniques are considered. Figure 7 illustrates the effect the bandwidth parameter has on the depth data estimates. Table 3 shows how the shortening magnitude S_C (eq. 10) is affected by the bandwidth parameter. An automated bandwidth selection method is relevant to balance the fit (getting the best precision for estimating the depth data) and the variance of the estimates. Cross-validation bandwidth selection method has been widely used in the infinite population context. We propose a new method for selecting the bandwidth parameter by taking into account the square root of the mean squared error (MSE) of the estimator and the length of the estimated folded surface. We select the bandwidth parameter h that minimizes the error measurements

$$E_1(h) = \sqrt{\frac{1}{n}\sum_{i=1}^{n}\left(Z_i - \widehat{m}_{\mathrm{np}}(x_i)\right)^2}, \tag{13}$$

and

$$E_2(h) = \sum_{i=1}^{n-1} \left|\Delta_{1i} + \Delta_{2i}\right|, \tag{14}$$

over a grid of values of the bandwidth parameter, with Δ_{1i} and Δ_{2i} the above-mentioned distances.

The cross-validation bandwidth selection method has also been taken into account for guiding reasons. Selection of the bandwidth parameter by using these two measurements makes sense from a statistical point of view, as the bandwidth parameter selected by minimizing the cross-validation function stays close to the one selected by the above-mentioned scores. This is illustrated for the seafloor and PS-b cases in Table 4, reinforcing clearly that the best bandwidth value in our case is 0.02 (cf., Fig. 5).

The precision on the fit of the underlying regression function is important from a geological point of view as it compromises fold magnitudes and in consequence, affects the reconstructed folding history. Table 5 compares for the different folded reflections the effect of the preferred nonparametric estimate ($h = 0.02$) with the best parametric estimator, illustrating how an incorrect specification of the regression model conditions, for example, the shortening S_C magnitude. We have shown that it has been an improvement over any handwritten measurement.

The nonparametric regression estimator $\widehat{m}_{\mathrm{np}}$ is expected to be the preferred estimator, since it does not place any restriction on the relationship between the auxiliary and the study variable. Table 6 shows the R_1 and R_2 values for the nonparametric regression smoother and the best parametric estimator. The nonparametric approach clearly dominates the parametric one.

These observations are also important because the nonparametric estimation conditions any further analysis of the folded surface, as for example the position of the fold hinge and the inflexion point in fold flanks.

Numerical results support the easy applicability of the method and its advantageous properties. The proposed method for selecting the bandwidth parameter seems to work well in this scenario and the kernel smoother adapted to discontinuities, describes the depth data scatter reasonably well. We may conclude that the use of nonparametric regression smoothers may be a good alternative to other classical parametric estimators.

6.2 Folding history

Fold Geometry Variations

The geometrical variation of the folded surfaces in the studied section is discussed using the relationships between their relative elevation with respect to the PS-bottom in the left-hand vertical of the profile (H_i) and the dip of the regional (α_i) (Fig. 7A). Additionally, the variations of the fold dip in the western and eastern limbs (β_1 and β_2, respectively) have been also plotted against H_i (Fig. 7B). The difference between both flanks is also included in this diagram.

The dip of the regional line that better fits the folded distribution diminishes continuously upward through the Productive Series. The best parametric fit for this distribution corresponds to a linear regression function ($r^2 = 0.95$), with a mean rate of 0.42°/km (Fig. 7A). Conversely, the dip angle for the youngest sediments, the post-PS sequence, shows a rather fluctuating distribution although it has a mean rate of approximately 0.96°/km.

According to these results, and using the time interval of both periods, we interpret that deposition of the Productive Series experienced a rather constant synsedimentary tilting of 0.15°/Ma. This process occurred as a subtle and continuous process in this margin of the SCB and promoted the basin subsidence of the PS thick sedimentary sequence (4.5 km) towards the East, where the basin is floored by a presumable oceanic crust (cf., Fig. 2; Berberian 1983; Mangino and Priestley 1998; Allen et al. 2002). During the last 3 my, coinciding with the deposition of the Akchagyl and Apsheron units, basin tilting accelerated to be around 0.31°/Ma.

With respect to the vertical variation of fold dips in the eastern and western flanks (Fig. 7B), it is inferred the occurrence of some other variations. For example, it is observed that the two flanks maintained the same attitude for the lower part of the PS sequence (from PS-b to H8 reflections), with a slight eastwards asymmetry or vergence, because the eastern limb dips approximately 10° more than the western one. The situation reverses during the uppermost PS sequences (from H8 to PS-top reflections) and the eastern limb diminishes progressively its dip, whereas the western limb remains with a constant attitude. During the post-PS sequence, with two clear sedimentary wedges in both flanks and abundant onlapping geometries (Fig. 3B), the observations depict

a slightly different scenario. The eastern flank has then a rather constant dip (∼7-10°), whereas the western limb tends clearly to smooth upwards (from 30° to 4-5°).

These observations lead us to interpret that the eastern limb acted as a leading flank at the onset of deformation and during the most recent epochs (i.e., the post-PS period). It is also inferred that around the H8 reflection it occurred a change in the deformation history. The inspection of the shortening magnitudes would help to complement these preliminary interpretations.

Folding History and Shortening Magnitudes

The two shortening magnitudes computed here, the curvimetric (S_C; equation 10) and the planimetric estimates (S_A; equations 11 and 12) are shown graphically in Figure 8 and their values are detailed in Table 2.

The planimetric shortening is commonly presented in a crossplot of the relative elevation (H_i) against the areas (A_i), and it corresponds there to the slope of the line connecting the observations with the inferred depth of the detachment surface (Fig. 1B). In the studied fold, the resultant H_i-A_i crossplot is shown in Figure 8A, where it has been also included the best linear and polynomial fit of the distributions interpreted as the pre- and syn-growth epochs.

This diagram demonstrates that the folding history is marked by two main episodes. Most of the Productive Series is a clear candidate to represent the pre-growth section, because it shows an increasing, and nearly linear relationship between A_i and H_i. This is better reproduced by a polynomial fit, in agreement to the findings of Gonzalez-Mieres and Suppe (2006). The maximum of this plot occurs within upper part of the Productive Series; i.e. around the H8 reflection. Within the overlying sequences, it is inferred the existence of two periods. Firstly, the slope of the A_i-H_i trend diminishes within the package formed by the uppermost Productive Series (from H8 to PS-top reflections), whereas the post-PS units, up to the seafloor, shows a continuous and decreasing relationship in the diagram (Fig. 8A).

The pre-growth sequence shows nevertheless an interesting convex shape in the A_i-H_i plot (Fig. 8A). We can rule out the occurrence of a significant layer-parallel shear during folding, because this process has been demonstrated to produce a reverse, concave upward relationship (e.g., Gonzalez-Mieres and Suppe 2006, 2011). In our case, the convex trend in the diagram might suggest the occurrence of volume changes during folding, due probably to subcompaction of the pre-growth sequence during burial or by lateral flow of the fluid- and shale-rich sediments.

According to the relationships observed in the A_i-H_i diagram, we suggest that the H8 reflection separate pre- and syn-growth intervals. Although in some circumstances fold growth could initiate below the maximum point in an A_i-H_i plot (e.g., Hubert-Ferrari et al. 2007; Gonzalez-Mieres and Suppe 2011), in our case the lack of a significant variation of the sedimentary thickness in the pre-H8 sequences between both flanks reinforces this interpretation. In consequence, and in spite of the clear wedges geometries depicted by the post-

PS sequences, the fold growth initiated previously, starting just before the age of the regional unconformity marked by the PS-top reflection. Extrapolating linearly the age of the PS-top and PS-surfaces; i.e., 5.9 and ∼3.1 Ma, respectively (e.g., Inan et al. 1997; Abreu and Nummedal 2007; Forte et al. 2014), we estimate that H8 has an approximate age of 3.5-3.4 Ma. In this section of the studied fold, this is the estimated time for the onset of folding. The syngrowth folding extends henceforth to Present (Fig. 8A).

The two periods identified within the growth interval are separated by the regional unconformity corresponding to the PS-top surface. The older growth episode occurred during deposition of the post-H8 Productive Series; i.e., from 3.5-3.4 to 3.1-3.2 Ma, and it coincides with a sudden increase of the sedimentation rates (av. 3.25 mm/yr). The temporal coincidence between fold growth and high sedimentation rates would help to explain that these sequences do not show a marked thinning towards the anticline crest (Fig. 3).

Conversely, the second episode of growth is clearly marked by the progressive thinning, and even the onlap geometries observed in the post-PS sediments towards the anticline crest. According to the geometries observed in these sediments, the fold uplift rate was nearly equal to the sedimentation rate during deposition of the Akchagyl Unit; i.e., between 3.1 to 1.6 Ma, because the fold crest was tapered by a thin sequence of these sediments (Fig. 3B). These are the common geometries formed when the synchronous sedimentation rate equals or lowers the fold uplift magnitude (e.g., Poblet et al. 1997). As the Akchagyl Unit covers always the anticline crest, it has not been necessary to apply the technique described by Poblet et al. (2004) to correctly estimate there the S_C shortening magnitude. For the post-PS period, we have obtained an average sedimentation rate of 0.66 mm/yr.

The area-to-depth graph can be also used to estimate the depth of the detachment surface (Fig. 1). We infer that the detachment surface or layer is situated at around 9.6 km depth (Fig. 8A), below the maximum depth illuminated by this seismic dataset. According to the regional knowledge, this estimate could coincide with the position of the Maykop Unit in this margin of the South Caspian Basin (e.g., Baganz et al. 2012). This unit is formed by clay-rich sediments with a high fluid-content (e.g., Buryakovsky et al. 1995; Hudson et al. 2008), and is known to be the source for the abundant mud diapirs and mud volcanoes in the South Caspian region (e.g., Stewart and Davies 2006; Roberts et al. 2010). All these characteristics, alike the seismic observations conducted in nearby areas (e.g. Fowler et al. 2000), reinforce our suggestion that the Maykop Unit acted as a mobile and weak unit during folding in this basin margin.

Regarding our reconstruction of the deformation magnitude in the section, the planimetric shortening (S_A, equations 11 and 12) registered by the pre-growth section (up to H8) corresponds to the total shortening at the beginning of fold growth; i.e., where dA_i/dH_i equals to cero (Gonzalez-Mieres and Suppe 2011). The relationship in this pre-growth section is better fitted by a polynomial function than with a linear regression. Using the polynomial regression

function, the mean shortening S_A for for the top of the pre-growth section results to be 1.16 ±0.09 km (Fig. 8B and Table 2).

The initial growth, corresponding to the H8 to PS-top interval, has a resulting average rate of shortening dS_A/dH equal to 0.19. The post-PS sequence has an associated dS_A/dH trend with a linear slope of 0.66 ±0.2 mm/yr. Within this sequence we have computed individual dS_A/dH values for the different units, resulting average values of 0.77 mm/yr for the Akchagyl Unit (3.1-1.6 Ma), 0.63 mm/yr for the Apsheron Unit (1.6-0.7 Ma), and lowering up to 0.43 mm/yr for the most recent sediments (<0.7 Ma). All these estimates indicate that the folding rate accelerated during the Akchagyl-to-Apsheron epoch of fold growth (3.1-0.7 Ma), simultaneously to a decrease in the sedimentation rates (av. 0.66 ±0.2 mm/yr).

Using our reconstruction of the age of the H8 reflection (3.5-3.4 Ma) and the values used regionally for the PS-top (3.1 Ma) and the Akchagyl and Apsheron units (1.6 and 0.7 Ma, respectively), we obtained average sedimentation rates in the western syncline of 3.24 mm/yr for the H8 to PS-top interval, and a rather low but increasing sedimentation rate during the second growth episode. For the latter epoch, it is inferred values of 0.22 and 0.60-0.66 mm/yr for the Akchagyl and for the Apsheron to Recent units, respectively (Soto et al. 2011).

Combining these estimates with the corresponding dS_A/dH values, it is inferred a punctuated history of deformation with diverse shortening rates (dS_A/dt), although they tend to decrease through the growth period. The first growth period, from H8 to PS-top (i.e., during 0.3-0.4 my), occurred under a shortening rate of 0.61 mm/yr, whereas the average rate during the post-PS epoch was of about 0.30 mm/yr. During the last 3.1 my, fold growth occurred under variable circumstances. During the first period, with a total duration of 1.5 my and coinciding with the deposition of the Akchagyl Unit (3.1-1.6 Ma), the resulting shortening rate (0.17 mm/yr) was rather similar to the sedimentation rate (0.22 mm/yr). Shortening rates increased to 0.37 mm/yr during deposition of the Apsheron Unit (1.6-0.7 Ma), which has an average sedimentation rate of 0.60 mm/yr. The situation for the most recent sediments (<0.7 Ma) shows a decreasing shortening (0.29 mm/yr) and a slight increase in the sedimentation rate (0.66 mm/yr).

These values explain the contrasting geometries identified within the growth sediments (Fig. 3); i.e., the imperceptible thinning of the upper PS sequences towards the anticline (i.e., $dS_A/dt << dz/dt$), the general onlap geometry identified in the Akchagyl Unit (i.e., $dS_A/dt \sim dz/dt$) and the drapping relationships and a smoother fold from the Apsheron to the most recent sediments ($dS_A/dt < dz/dt$).

The comparison between the shortening magnitudes S_C and S_A gives finally some interesting details to the folding history of this structure. In this case, the curvimetric shortening (S_C) is always significantly lower than the shortening estimated through the A_i-H_i relationships (S_A; Fig. 8B). This difference tends to diminish upwards within the pre- and syn-growth sequences, varying monotonically from ∼3.5 km in the lower portion of the PS to 0.4-0.1 km in the Apsheron and the seafloor. Similar differences have also been found

in other folds of this type (Gonzalez-Mieres and Suppe 2006). This is indicating that this fold does not conserve bed length, and certainly suggests the occurrence of a volume increase during shortening. This process accompanied the deformation of a thick sequence with interlayered sand and shale intervals, which could therefore release (or retain) fluids during folding. In this context, the out-of-plane mobilization of weak layers as the buried Maykop Unit, could promote an inflation or upwelling of the fold core during shortening. These types of processes are relatively common in salt-cored anticlines (e.g. Rowan 1997; Rowan et al. 2000), and the studied fold in the South Caspian Basin constitutes therefore a comparable structure in a case feed by overpressured shales.

7 Conclusions

(1) The nonparametric regression results to be a powerful technique to reconstruct the complete shape of an active, NW-SE fold in the western South Caspian Basin (offshore Azerbaijan). Using a detailed seismic interpretation of a depth-migrated seismic line, the different horizons have been exported and fit with different bandwidth values (h) of the nonparametric estimate. The studied fold is better smoothed with $h = 0.02$. We have demonstrated that this method is able also to work with discontinuities in the folded horizons and produces always a much better fit than the best parametric estimate. Additionally, different error measurements have been developed here to estimate the accuracy of the method.

(2) The complete shape of a numerous set of deformed horizons in the fold has been characterized by measuring different parameters through a robust software tool (R). We have implemented our own code in the programming language R for estimating discontinuous depth data. The main variables are: the total length of the deformed surface; the position of the maximum and minima of the distribution, which coincides with the anticline crest and the syncline troughs, respectively; and the location of the inflection points and the dip of the fold flanks in their vicinities. We have also estimate the best linear fit of the folded surface, the length and dip of this line of (or regional), alike the areas encompassed by the folded surface and their regional line. With the latter variables, we have computed the curvimetric (S_C) and the planimetric shortening (S_A), which is based in the relationships between folded areas (A_i) and their relative elevation (H_i), using the method of Gonzalez-Mieres and Suppe (2006, 2011).

(3) The overall geometry of the structure corresponds to an active detachment fold with a buried detachment surface (or layer) situated at about 9.6 km depth. It is suggested that this level occurs within a weak and mud-rich layer, which is known regionally as the Maykop Unit. The fold structure deforms the Productive Series (5.9 to ∼3.4-3.1 Ma) and above a regional unconformity (the PS-top reflection), it lays a younger sequence of sedi-

ments that include the Akchagyl and Apsheron units (3.1-1.6 and 1.6-0.7 Ma, respectively).

(4) Some of the observations conducted in this fold describes a geometry that departs slightly from the detachment fold-type; mainly, because it has been reconstructed a long-lived history of basinward tilting accompanying sedimentation and folding, which accelerated from 0.15°/Ma to 0.31°/Ma after deposition of the Productive Series. In addition, we have evaluated the vertical variation of the fold vergence and the limb angles, identifying a varied position of the leading flank. It is interpreted that the leading flank was mostly the eastern limb, but it loosed prominence and the anticline became more symmetric during the onset of fold growth.

(5) The relationships between the folded area and elevation (A_i-H_i crossplot) have demonstrated the occurrence of two growth episodes, and suggest that the pre-growth sequence correspond to the middle- to-lower PS sequence (i.e., situated below the H8 reflection; ca. 3.4 Ma). The older one, occurred just before the regional PS unconformity, from 3.5-3.4 to ∼3.1 Ma and has an associated shortening rate dS_A/dH_i of 0.19. The most conspicuous growth occurred henceforth, during the deposition of the post-PS sequences ($<$ 3.1 Ma), with an average dS_A/dH_i rate of 0.58. During this epoch, dS_A/dH_i rate varies from 0.77 for the Akchagyl Unit (3.1-1.6 Ma), 0.63 for the Apsheron Unit (1.6-0.7 Ma), and 0.43 for the most recent sediments.

(6) The age of the different sedimentary sequences have been used to reconstruct the sedimentation rates during fold growth, resulting average values of 3.24 mm/yr for the uppermost PS units, whereas within the post-PS sequences they varied from 0.22 to 0.66± 0.08 mm/yr for the Akchagyl and the Apsheron to Recent sediments, respectively.

(7) Combining the sedimentation rates and the dS_A/dH_i values, we have reconstructed the shortening rate magnitudes (dS_A/dt) during the fold growth. Folding started at 3.5-3.4 Ma with a relatively low shortening rate of 0.2 mm/yr and an extremely high sedimentation rate (3.24 mm/yr). During the second stage of fold growth, shortening rate decreased up to 0.17 mm/yr during the deposition of the Akchagyl Unit (±3.1-1.6 Ma) and a major shortening pulse with a rate of 0.37 mm/yr ocurred during the deposition of the Apsheron Unit (1.6-0.7 Ma), decreasing afterwards its magnitude to 0.29 mm/yr up to Recent (i.e., $<$0.7 Ma). In consequence, the balance between sedimentation and shortening rates varies during folding, explaining the contrasting geometries (flank wedges vs. tapering) observed in the growth sediments.

(8) Curvimetric shortening (S_C) is significantly lower than the estimate given by the area-to-depth relationships (planimetric shortening, S_A). This difference is indicating that this fold does not conserve bed length and volume during deformation. We postulate the occurrence also of out-of-plane flow of overpressured mud-rich sediments that inflate the fold core during shortening, similarly to the upwelling processes commonly found in salt-cored anticlines.

Acknowledgements The authors would like to thank REPSOL Exploración, S.A. for kindly providing the data and financial support to conduct this study. This research was also financed by MICINN research projects TRA2009-0205 and MTM2009-10055 (Spain). This is a contribution from the research groups FQM365 and RNM376 of the Junta de Andalucía in Spain. Seismic interpretation has been conducted with KingdomSuite. This software is kindly provided by IHS through an academic agreement with the Granada University.

References

1. Abdullayev, NR (2000) Seismic stratigraphy of the Upper Pliocene and Quaternarydeposits in the South Caspian Basin. J Petrol Sci Eng 28:207–226
2. Abreu V, Nummedal D (2007) Miocene to Quaternary sequence stratigraphy of the South and Central Caspian Basin. In: Yilmaz PO, Isaksen GH (eds) Oil and gas of the Greater Caspian Sea: Studies in Geology 55:65–86
3. Allen MB, Jones S, Ismail-Zadeh A, Simmons M, Anderson, L (2002) Onset of subduction as the cause of rapid Pliocene-Quaternary subsidence in the South Caspian basin. Geol Soc Am Bull 30:775–778
4. Allen MB, Vincent SJ, Alsop GI, Ismail-zadeh A, Flecker R (2003) Late Cenozoic deformation in the South Caspian region: effects of a rigid basement block within a collision zone. Tectonophysics 366:223–239
5. Antoniadis, A (1997) Wavelets in statistics: a review (with discussion). Stat Methods Appl 6:97-144
6. Baganz OW, Bagirov E, Michael GE, Shultz A (2012) Productive series play of the Paleo-Volga Delta, South Caspian Basin: Exploration history, sedimentation, and petroleum system. In Baganz OW, Bartov Y, Bohacs K, Nummedal D (eds) Lacustrine sandstone reservoirs and hydrocarbon systems AAPG Memoir 95:57–70. doi: 10.1306/13291384M953444
7. Bagirov E, Nadirov R, Lerche I (1997) Hydrocarbon evolution for a north-south section of the South Caspian Basin. Mar Petrol Geol 14:773–854
8. van Baak CGC, Vasiliev I, Stoica M, Kuiper KF, Forte AM, Aliyeva E, Krijgsman W (2013) A magnetostratigraphic time frame for Plio-Pleistocene transgressions in the South Caspian Basin, Azerbaijan. Global Planet Change 103:119-134. doi: 10.1016/j.gloplacha.2012.05.004
9. Berberian M (1983) The southern Caspian: a compressional depression floored by a trapped, modified oceanic crust. Can J Earth Sci 20:163–183
10. Bowman AW, Pope A, Ismail B (2006) Detecting discontinuities in nonparametric regression curves and surfaces. Stat Comput 16:377–390
11. Breidt J, Opsomer, J (2000) Local Polynomial Regression estimators in survey sampling. Ann Stat 28:1026-1053
12. Brunet MF, Korotaev MV, Ershov, AV, Nikishin, AM (2003) The South Caspian Basin: a review of its evolution from subsidence modelling. Sediment Geol 156:119–148
13. Buryakovsky LA, Djevanshir RD, Chilingar GV (1995) Abnormally-high formation pressures in Azerbaijanand the South Caspian Basin (as related to smectite-illite transformations during diagenesis and catagenesis). J Petrol Sci Eng 13:203–218
14. Chamberlin RT (1910) The Appalachian folds of central Pennsylvania. J Geol 18:228–251
15. Dahlstrom CDA (1969) The upper detachment in concentric folding. B Can Petrol Geol 17:326–346
16. Dahlstrom CDA (1990) Geometric constraints derived from the law of conservation of volume and applied to evolutionary models for detachment folding. AAPG Bull 74:336–344
17. Devlin WJ, Cogswell JM, Gaskins GM, Isaksen GH, Pitcher DM, Puls DP, Stanley KO, Wall, GRT (1999) South Caspian Basin: young, cool, and full of promise. The Geological Society of America Today 9:1–9
18. EIA (2013) Overview of oil and natural gas in the Caspian Sea region. U.S. Energy Information Administration
19. Epard JL, Groshong RHJ (1993) Excess area and depth to detachment. Am Assoc Petr Geol B 77:1291–1302

20. Fan, J (1992) Design-adaptive nonparametric regression. J Am Stat Assoc 87:9981004
21. Fan, J (1993) Local linear regression smoothers and their minimax efficiencies. Ann Stat 21:196-216
22. Fan J, Gijbels I (1996) Local Polynomial Modelling and its Applications. Chapman & Hall, London
23. Fowler SR, Mildenhall J, Zalova S, Riley G, Elsley G, Desplanques A, Guliyev F (2000) Mud volcanoes and structural development on Shah Deniz. J Petrol Sci Eng 28:189–206
24. Forte AM, Sumner DY, Cowgill E, Stoica M, Murtuzayev I, Kangarli T, Elashvili M, Godoladze T, Javakhishvili A (2014) Late Miocene to Pliocene stratigraphy of the Kura Basin, a subbasin of the South Caspian Basin: implications for the diachroneity of stage boundaries. Basin Res 26:1–25. doi: 10.1111/bre.12069
25. Gonzalez-Mieres R, Suppe J (2006) Relief and shortening in detachment folds. J Struct Geol 28:1785–1807
26. Gonzalez-Mieres R, Suppe J (2011) Shortening histories in active detachment folds based on area-of-relief methods. In McClay K, Shaw J, Suppe J (eds) Thrust fault-related folding. AAPG Memoir 94:39–67. doi: 10.1306/13251332M943428
27. Guest B, Guest A, Axen G. (2007) Late Tertiary tectonic evolution of northern Iran: a case for simple crustal folding. Global Planet Change 58:435–453
28. Hinds DJ, Aliyeva E, Allen, MB, Davies CE, Kroonenberg SB, Simmons MD, Vincent SJ (2004) Sedimentation in a discharge dominated fluvial-lacustrine system: the Neogene Productive Series of the South Caspian Basin, Azerbaijan. Mar Petrol Geol 21:613–638. doi: 10.1016/j.tecto.2007.11.045
29. Hubert-Ferrari A, Suppe J, Gonzalez-Mieres R, Wang S (2007) Mechanisms of active folding of the landscape (southern Tian Shan, China). J Geophys Res 112 B03S09. doi:10.1029/2006JB004362
30. Hudson SM, Johnson CL, Efendiyeva MA, Rowe HD, Feyzullayev AA, Aliyev CS (2008) Stratigraphy and geochemical characterization of the Oligocene Miocene Maikop series: Implications for the paleogeography of Eastern Azerbaijan. Tectonophysics 451:40–55
31. Inan S, Yalçin MN, Guliev IS, Kuliev K, Feizullayev AA (1997) Deep petroleum occurrences in the Lower Kura Depression, South Caspian Basin, Azerbaijan: an organic geochemical and basin modeling study. Mar Petrol Geol 14:731–762
32. Jackson J, Priestley K, Allen MB, Berberian M (2002) Active tectonics of the South Caspian Basin. Geophys J Int 148:214–245
33. Jones RW, Simmons, MD (1997) A review of the stratigraphy of Eastern Paratethys (Oligocene-Holocene), with particular emphasis on the Black Sea. In Robinson, A.G. (eds), Regional and petroleum geology of the Black Sea and surrounding region. AAPG Memoir 68:39–52
34. Loader C (1999) Change point estimation using nonparametric regression. Ann Stat 27:1667-1678
35. Mangino S, Priestley K (1998) The crustal structure of the southern Caspian region. Geophys J Int 133:630–648
36. Mitra S (2002) Fold-accommodation faults. AAPG Bull 86:671–693
37. Mitra S (2002) Structural models of faulted detachment folds. AAPG Bull 86:1673–1694
38. Mitra S (2003) A unified kinematic model for the evolution of detachment folds. J Struct Geol 25:1659–1673
39. Mitra S, Namson J (1989) Equal-area balancing. Am J Sci 289:563–599
40. Morton A, Allen M, Simmons M, Spathopoulos F, Still J, Hinds D, Ismail-Zadehz A, Kroonenberg S (2003) Provenance patterns in a Neotectonic basin:Plioceneand Quaternary sediment supply to the SouthCaspian. Basin Res 15:321–337
41. Nadirov RS, Bagirov E, Tagiyev M, Lerche I (1997) Flexural plate subsidence, sedimentation rates, and structural development of the super-deep South Caspian Basin. Mar Petrol Geol 14:383–400
42. Narimanov AA (1993) The petroleum systems of the South Caspian Basin, in Doré, AG et al. (eds) Basin Modelling Advances and Applications. NPF Special Publication 3:599–608
43. Neprochnov YP (1968) Structure of the earths crust of epi-continental seas: Caspian, Black, and Mediterranean. Can J Earth Sci 5:1037–1043
44. Percival D, Walden A (2000) Wavelet Methods for Time Series Analysis. Cambridge University Press

45. Poblet J, McClay K (1996) Geometry and kinematics of single-layer detachment folds. AAPG Bull 80:1085–1109
46. Poblet J, McClay K, Storti F, Muoz JA (1997) Geometries of syntectonic sediments associated with single-layer detachment folds. J Struct Geol 19:369–381
47. Poblet J, Bulnes M, McClay K, Hardy S (2004). Plots of crestal structural relief and fold area versus shortening-A graphical technique to unravel the kinematics of thrust-related folds. In McClay, KR (ed) Thrust tectonics and hydrocarbon systems. AAPG Memoir 82:372–399
48. Priestley MB, Chao MT (1972) Nonparametric function fitting. J Roy Stat Soc B 34:385-392
49. Ramsay JG, Huber MI (1987) The techniques of modern structural geology. Volume 2: Folds and Fractures. Academic Press 400. London
50. Roberts KS, Davies RJ and Stewart SA (2010) Structure of exhumed mud volcano feeder complexes, Azerbaijan. Basin Res 22:439–451. doi: 10.1111/j.1365-2117.2009.00441.x
51. Rowan MG (1997) Three-dimensional geometry and evolution of a segmented detachment fold, Mississippi Fan foldbelt, Gulf of Mexico. J Struct Geol 19:463–480
52. Rowan MG, Trudgill BD, Fiduk JC (2000) Deep-water, salt-cored foldbelts: leassons from the Mississipi Fan and Perdido Fold belts, Northern Gulf of Mexico. In Mohriak W, Talwani M (eds). Atlantic Rifs and Continental Margins. American Geophysical Union, Geophysical Monograph 115:173–191
53. Ruppert D, Wand MP (1994) Multivariate locally weighted least squares regression. Ann Stat 22:1346-1370
54. Ruppert D, Wand MP, Carroll RJ (2003) Semiparametric Regression. Cambridge University Press, Cambridge, UK
55. Sánchez-Borrego I, Martinez-Miranda MD, González-Carmona A (2006) Local linear kernel estimation of the discontinuous regression function. Computation Stat 21:557-569
56. Shikalibeily ES, Grigoriants BV (1980) Principal features of the crustal structure of the South-Caspian basin and the conditions of its formation. Tectonophysics 69:113–121
57. Smith-Rouch LS (2006) OligoceneMiocene Maykop/Diatom total petroleum system of the South Caspian Basin Province, Azerbaijan, Iran, and Turkmenistan. U.S. Geological Survey Bulletin 2201I:1–27
58. Soto JI, Santos-Betancor I, Sánchez Borrego IR, Macellari, CE (2011) Shale diapirism and associated folding history in the South Caspian Basin (offshore Azerbaijan). AAPG Annual Convention and Exhibition, Houston, Texas. Search and Discovery Article #30162
59. Stewart SA, Davies RJ (2006) Structure and emplacement of mud volcano systems in the South Caspian Basin. AAPG Bull 90:771–786
60. Wiltschko DV, Groshong RH Jr (2012) The Chamberlin 1910 balanced section: Context, contribution, and critical reassessment. J Struct Geol 41:7–23. doi: 10.1016/j.jsg.2012.01.019
61. Wu J, Chu C (1993) Nonparametric function estimation and bandwidth selection for discontinuous regression functions. Stat Sinica 3:557-576
62. Yusifov M, Rabinowitz PD (2004) Classification of mud volcanoes in the South Caspian Basin,offshore Azerbaijan. Mar Petrol Geol 21:965–975. doi: 10.1016/j.marpetgeo.2004.06.002
63. Zonenshain LP, Le Pichon X (1986) Deep basins of the Black Sea and Caspian Sea as remnants ofMesozoic back-arc basins. Tectonophysics 123: 181–211

Table 1 List of magnitudes

Z_i	Horizon depth from the sea surface
H_i	Horizon elevation above the PS-b surface
L_i	Initial length of the estimated folded surface
L_f	Final length of the surface in the deformed situation
r^2	Coefficient of determination of the fits
α	Angle between the regional line and the horizontal axis (regional dip)
β_1	Angle between the tangent to the estimated surface at the first inflexion point and the horizontal axis (dip of the W-fold limb)
β_2	Angle between the tangent to the estimated surface at the second inflexion point and the horizontal axis (dip of the E-fold limb)
S_C	Curvimetric shortening
S_A	Planimetric shortening

Table 2 Magnitudes values of the fold section. Shortening values in m. S_A calculated using the inferred position of the detachment surface (ca. Polynomial fit)

Horizon	Z_i (m)	H_i (m)	L_i (m)	L_f (m)	r^2	α (°)	β_1 (°)	β_2 (°)	S_C (m)	S_A (m)
sf	616.5	5955.5	13125.6	13109.5	0.9987	0.940	3.4	6.1	16.11	111.37
Ap1	957.8	5614.1	13162.4	13109.3	0.9992	0.875	10.4	6.2	53.15	249.07
Ap2	1148.4	5423.6	13212.7	13111.5	0.9987	1,372	16.0	7.5	101.25	341.12
Ak1	1398.2	5173.7	13359.8	13112.7	0.9965	1.586	14.9	14.2	247.01	478.22
Ak2	1687.2	4884.7	13464.5	13112.2	0.9974	1.496	28.3	8.4	352.27	678.00
PS-t	1994.4	4577.5	13691.9	13118.6	0.9913	2.338	30.4	6.1	573.23	913.33
H10	2198.4	4373.5	13723.2	13117.7	0.9913	2.239	30.4	13.6	605.43	978.64
H9	2847.1	3724.8	13837.8	13123.5	0.9911	2,808	32.6	23.3	714.32	1095.29
H8	3296.3	3275.6	13939.9	13124.5	0.9903	2.901	31.2	22.7	815.33	1158.15
H7	3749.4	2822.5	14025.4	13126.1	0.9923	3.032	13.3	41.4	899.34	1242.96
H6	3982.9	2589.0	14075.3	13126.4	0.9933	3.056	15.6	29.1	948.94	1277.34
H5	4471.6	2100.3	14151.4	13128.5	0.9925	3.227	30.2	41.6	1022.87	1355.81
H4	4794.0	1777.9	14224.7	13130.9	0.9930	3.405	22.6	45.4	1093.79	1380.86
H3	5236.6	1335.3	14300.8	13132.7	0.9949	3,532	18.3	33.3	1168.16	1427.49
H2	5673.0	898.9	14252.5	13135.0	0.9930	3.692	16.5	34.3	1117.55	1530.17
H1	5985.8	586.2	14365.8	13136.4	0.9932	3.790	21.2	34.5	1229.31	1713.50
PS-b	6571.9	0.0	14241.3	13149.2	0.9944	4.553	22.8	34.4	1092.06	1626.04

Table 3 Effect of the bandwidth parameter on the curvimetric shortening magnitude S_C for the seafloor (sf) and the bottom of the Productive Series (PS-b) surfaces of the anticline shown in Figure 3.

		sf	PS-b
Estimator	h	S_C (m)	S_C (m)
$\widehat{m}_{\mathrm{np}}$	0.02	16.11	1092.06
	0.10	12.83	1055.47
	0.15	10.51	1052.67
	0.20	8.34	1045.35
	0.25	6.63	1039.81
	0.30	5.47	1033.56
$\widehat{m}_{\mathrm{par}}$		1.35	33.06

Table 4 Bandwidth parameter selection for the seafloor (sf) and the bottom of the Productive Series (PS-b) surfaces

		sf		PS-b	
Estimator	h	E_1	E_2	E_1	E_2
$\widehat{m}_{\mathrm{np}}$	0.02	2.196	17.393	5.480	348.030
	0.03	2.393	17.760	5.737	374.595
	0.04	2.660	17.759	10.714	389.783
	0.05	3.038	17.970	11.147	400.677
	0.06	3.497	18.075	11.535	411.474
$\widehat{m}_{\mathrm{par}}$		120.823	23.219	479.167	1274.604

Table 5 Curvimetric shortening value of estimators $\widehat{m}_{\mathrm{np}}$ and $\widehat{m}_{\mathrm{par}}$ for the deformed surfaces in the anticline shown in Figure 3.

Horizon	$\widehat{m}_{\mathrm{np}}$	$\widehat{m}_{\mathrm{par}}$	Handwriting
sf	16.11	1.35	25
Ap1	53.15	1.72	0
Ap2	101.25	4.05	
Ak1	247.01	5.62	275
Ak2	352.27	6.72	
PS-t	573.23	9.77	525
H10	605.43	11.15	525
H9	714.32	18.19	725
H8	815.33	21.09	750
H7	899.34	23.14	925
H6	948.94	25.72	925
H5	1022.87	26.16	1025
H4	1093.79	30.86	900
H3	1168.16	32.50	1100
H2	1117.55	31.93	1275
H1	1229.31	30.48	1150
PS-b	1092.06	33.23	1125

Table 6 Gain in efficiency in percent R_1 and R_2 of estimator $\widehat{m}_{\mathrm{np}}$ to $\widehat{m}_{\mathrm{par}}$ for the folded horizons shown in Figure 3.

Horizon	R_1	R_2
sf	5402.95	33.52
Ap1	6609.00	9.68
Ap2	3467.84	28.00
Ak1	5709.34	29.78
Ak2	17251.57	191.93
PS-t	4514.43	162.78
H10	10995.83	291.58
H9	8642.02	240.06
H8	9811.96	513.51
H7	9381.75	513.91
H6	8654.56	419.74
H5	7530.62	545.63
H4	6158.33	240.71
H3	4778.90	447.32
H2	8714.61	204.10
H1	12999.51	300.64
PS-b	8247.86	240.27

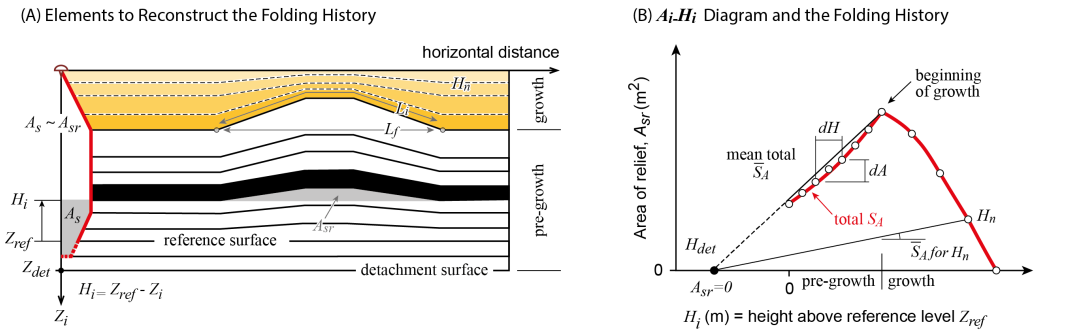

Figure 1 , Sanchez-Borrego et al.

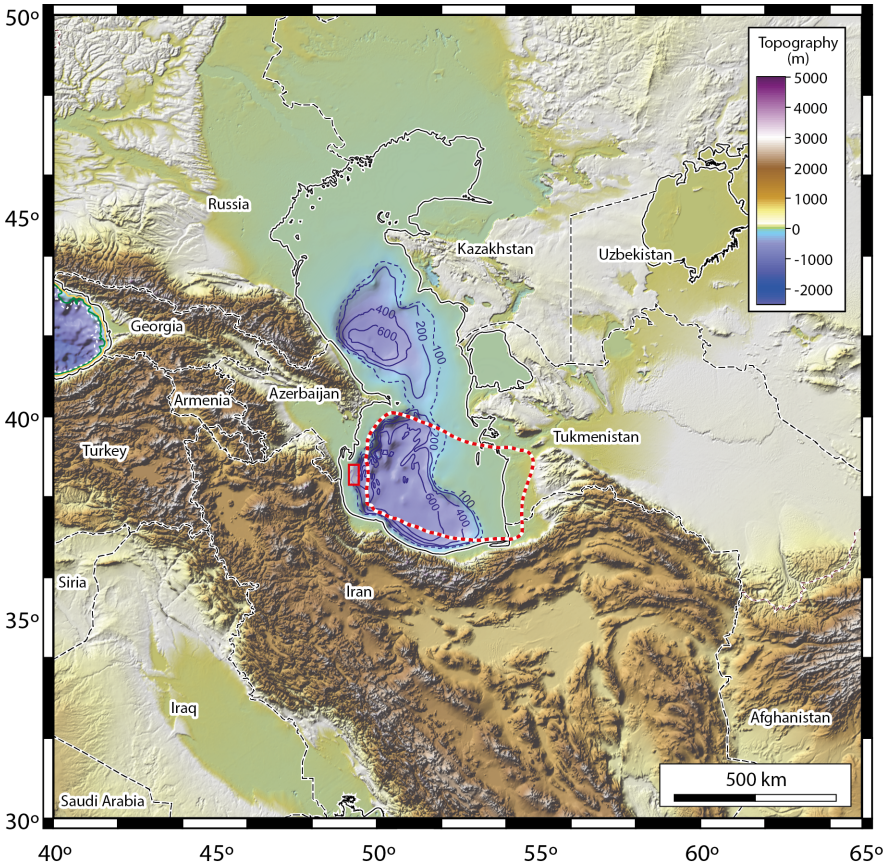

Figure 2 , Sanchez-Borrego et al.

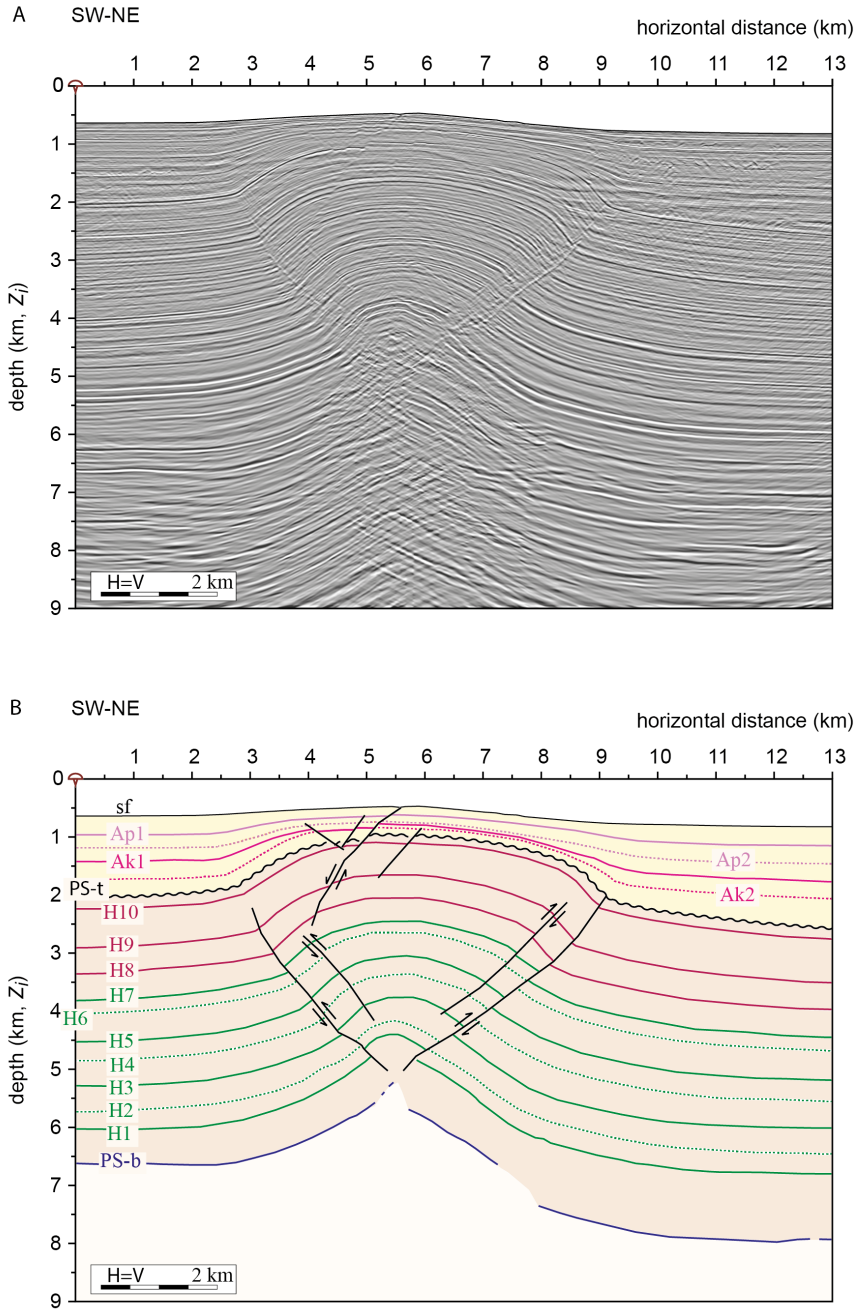

Figure 3 , Sanchez-Borrego et al.

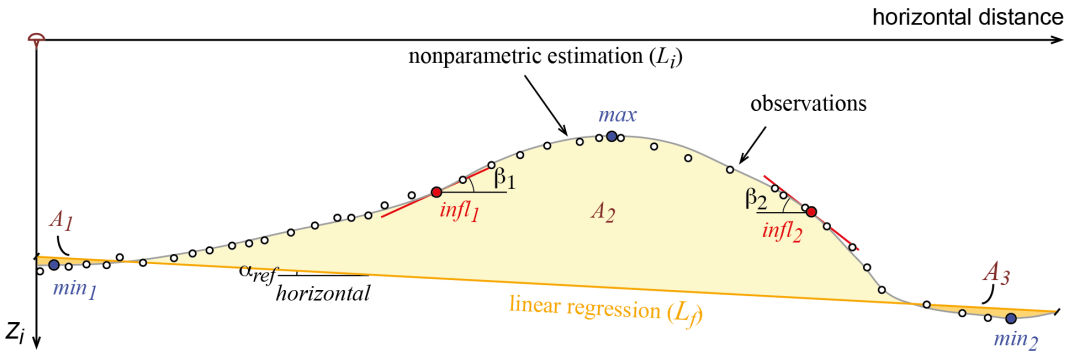

Figure 4 , Sanchez-Borrego et al.

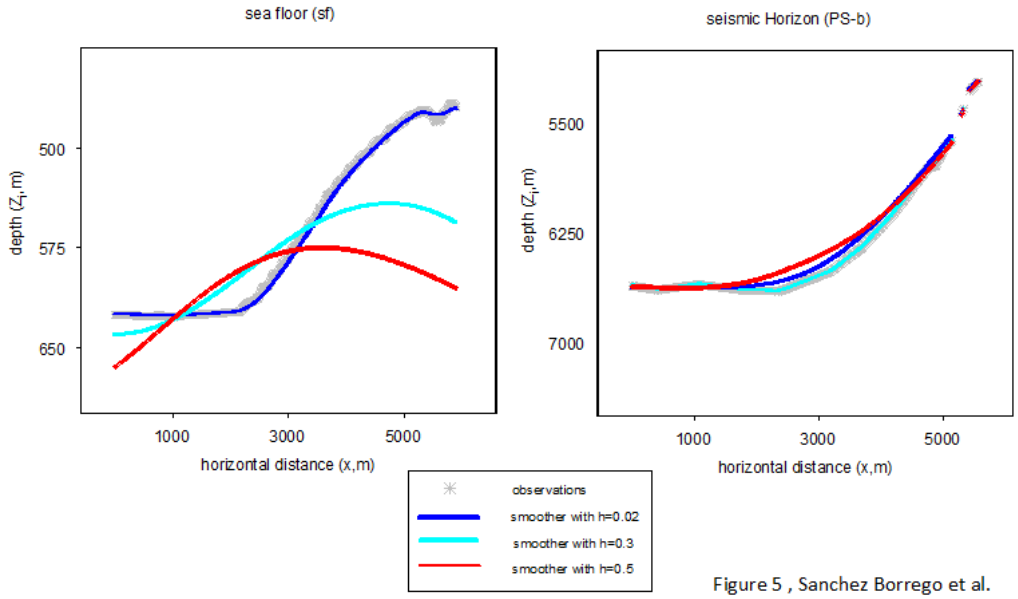

Figure 5 , Sanchez Borrego et al.

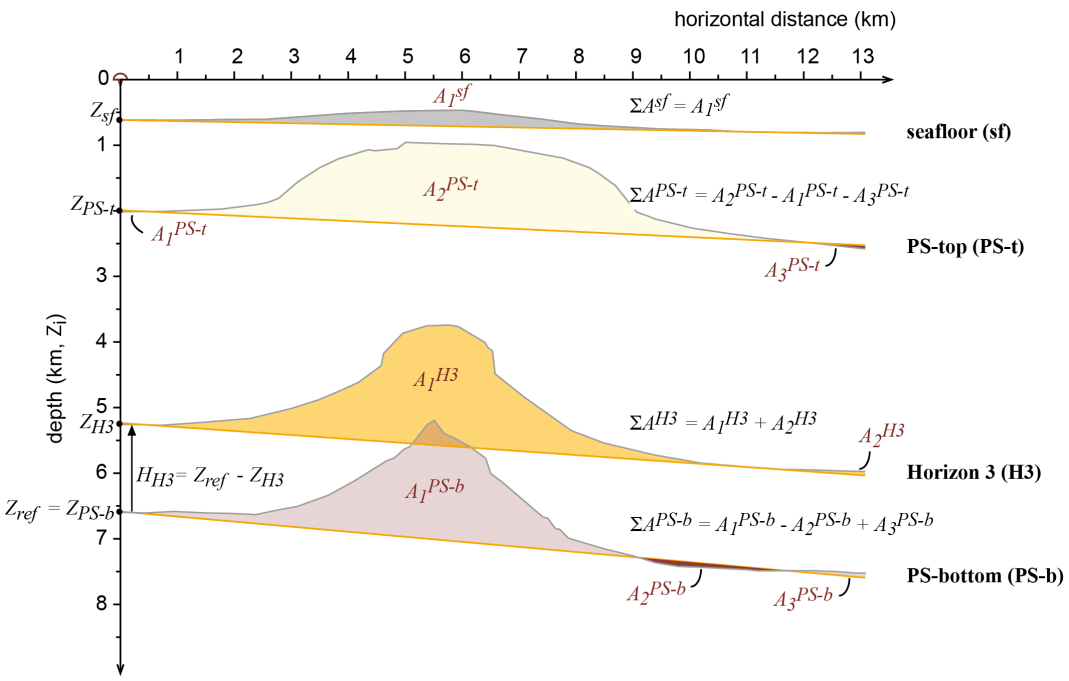

Figure 6 , Sanchez-Borrego et al.

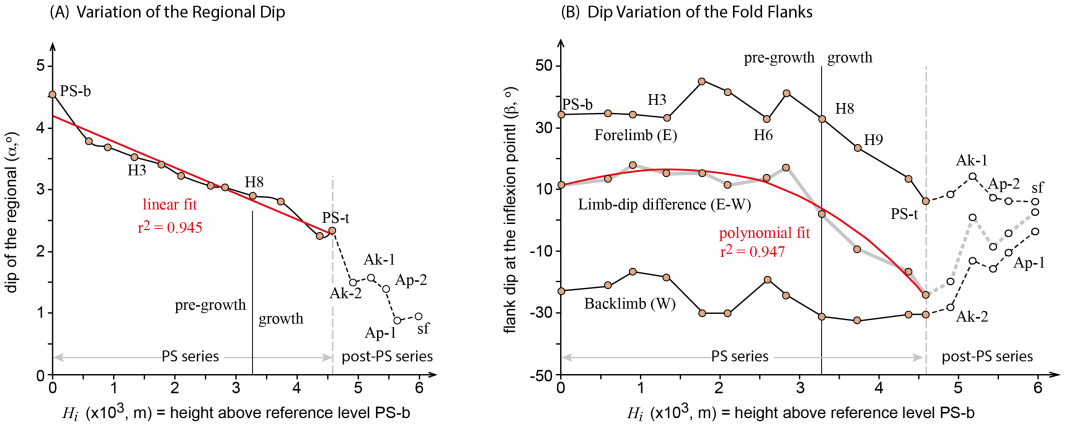

Figure 7 , Sanchez-Borrego et al.

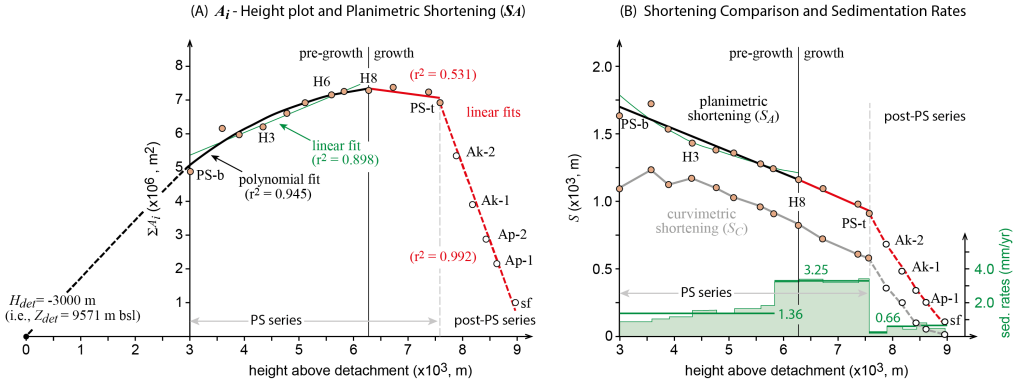

Figure 8 , Sanchez-Borrego et al.

Figure captions

Figure 1: Geometrical estimation of shortening in a detachment fold with pre- and syn-growth sequences, based on layer length variations and on depth-to-fold area relationships. Folding has some component of layer-parallel simple shear in the deeper levels of the pre-growth sequences. This figure is inspired in Gonzalez-Mieres and Suppe (2006, 2012). (**A**) Shortening is estimated as curvimetric (S_C) and planimetric (S_A), respectively. S_C results from the difference between initial length of the folded horizon (L_i) and final length measured along its regional or undeformed elevation (L_f). S_A is a function of the area of structural relief of the deformed horizon (A_{sr}) and the horizon height above a reference surface (H_i), located at depth Z_{ref}. A_{sr} is the deflection area of the folded horizon measured from its regional level, and it is equal to the area of shortening (A_s) in ideal folds. (**B**) Approximate plot of A_{sr} against relative heights H_i corresponding to the scheme shown in (A), illustrating how S_A can be estimated both in the pre- and syn-growth sequences (following Gonzalez-Mieres and Suppe, 2012). For simplification, it is assumed that the beginning of fold growth occurs at the maximum of this plot (see text for discussion). Along the A_{sr}-H_i trend, $A_{sr} = 0$ locates the height of the detachment surface with respect to the reference level (H_{det}).

Figure 2: Topographic map of the Caspian Sea and the surrounding mountain ranges. The red rectangle shows the position of the study area in offshore Azerbaijan, close to the Iran boundary, in shallow water depths (<100 m). Surface elevation is taken in onshore regions from etopo1-USGS database and bathymetry is from GEBCO 2008. Bathymetry contour range from 100 to 600 m below the relative sea level in the Caspian Sea, which is approximately 28 m below the global sea level. The discontinuous red line marks the oceanic-type crust in the South Caspian Basin (taken from Berberian 1983).

Figure 3: Non-interpreted (A) and interpreted (B) depth-migrated seismic section across the studied fold anticline. Seismic horizons correspond to the seafloor surface (sf), top of the Apsheron (Ap1) and Akchagyl units (Ak1), top and bottom of the Productive Series (PS-t and PS-b, respectively). Different seismic reflections identified within the Productive Series are labelled from H1 to H10. Within the Apsheron and Akchagyl units it is identified some internal, key reflections (Ap2 and Ak2, respectively). Reference vertical is pinned on the left hand side of the section. Vertical scale is in real depth (in meters) with no vertical exaggeration.

Figure 4: Scheme showing the fold elements estimated in this study. Abbreviations are described in Table 1. It is labelled the areas defined by the folded surface above (A_2) and below (A_1 and A_3) the regional surface. It is included the position of the inflexion points and the mean dip of the fold flanks ($infl_1$-β_1 and $infl_2$-β_2), like the maximum and minimum of the distribution, corresponding with the anticline and syncline crests, respectively.

Figure 5: Illustration of the effect that different values of the bandwidth parameter (h) has on the estimation of depth data for part of the seafloor (sf) and and H3 distributions from the anticline shown in Figure 3.

Figure 6: Examples of nonparametric estimation of selected reference horizons of the fold structure shown in Figure 3. Symbols like in Figures 1 and 4. Abbreviations appear listed in Table 1. Reference depth (Z_{ref}) is taken as the depth of the bottom of the Productive Series (PS-b) at the vertical on the left hand side of the section (values in Table 2).

Figure 7: Example of the fold elements computed through the nonparametric estimate of the structure shown in Figure 3. (**A**) Relationships between the dip of the regional (α) and the height above the reference level, represented by the PS-b surface (H_i). The best linear fit of the Productive Series (PS) is also included. (**B**) Variation of the limb dips with respect to the relative depth (H_i). It is compared the dip in the western (β_W or β_1) and the eastern (β_E or β_2) limbs. The difference between both magnitudes is also included to illustrate subtle variations in the fold style.For the PS sequence, plotted as a continuous thick line, the best fit corresponds to a polynomial function. The appropriate coefficient of determination (r^2) is included for reference in both plots. Horizon labels according to Figure 3. Other abbreviations are listed in Table 1.

Figure 8: Shortening estimates in the studied fold structure (Fig. 3) according to the nonparametric estimate for the different surfaces. (**A**) Relationships between the structural relief (A_{sr}) and the height above the estimated detachment level. It is also included the linear and polynomial fits of the pre-growth sequence, within the Productive Series (PS), and the best linear fits for the two interpreted periods of fold growth. In all the cases it is included their coefficient of determination (r^2). The estimated depth of the detachment surface for the section is ±9.6 below sea level (bsl; i.e., H_{det}= -3.0 km). (**B**) Plot showing the variation of the shortening magnitude with the height above the estimated detachment level. It is also included the sedimentation rates (in mm/yr) calculated in this study (green, horizontal bars) and the detailed values computed with the confidential stratigraphic information provided by REPSOL Exploración, S.A. (pale green histogram). It is compared the curvimetric (S_C) and the planimetric (S_A) shortening estimates, and the appropriate trends corresponding to the linear and polynomial fits shown in (A). For the latter case, it is also included the results according to the linear and polynomial fits of the S_A distribution for the PS sequences shown in (A). Horizon labels according to Figure 3. Other abbreviations are listed in Table 1.

Table captions

Table 1: List of magnitudes.

Table 2: Magnitudes values of the fold section.

Table 3: Effects of the bandwidth parameter on the curvimetric shortening magnitude SC for the seafloor (sf) and the bottom of the Productive Series (PS-b) surfaces of the anticline shown in Figure 3.

Table 4: Bandwidth parameter selection for the seafloor (sf) and the bottom of the Productive Series (PS-b) surfaces. The nonparametric estimates are also compared to the best parametric fit. $h = 0.02$ is selected by minimizing E_1 and E_2 scores.

Table 5: Curvimetric (S_C) shortening value of estimators $\widehat{m}_{\mathrm{np}}$ and $\widehat{m}_{\mathrm{par}}$ for the deformed surfaces in the anticline shown in Figure 3. It is included for comparison the SC values obtained by handwriting.

Table 6: Gain in efficiency in percent R_1 and R_2 of estimator $\widehat{m}_{\mathrm{np}}$ to $\widehat{m}_{\mathrm{par}}$ for the fold section shown in Figure 3.